Simultaneous *in vivo* positron emission tomography and magnetic resonance imaging

Ciprian Catana*†, Daniel Procissi‡, Yibao Wu*, Martin S. Judenhofer§, Jinyi Qi*, Bernd J. Pichler§, Russell E. Jacobs‡, and Simon R. Cherry*

*Department of Biomedical Engineering, University of California, Genome and Biomedical Sciences Facility, 451 East Health Sciences Drive, Davis, CA 95616; ‡Beckman Institute, California Institute of Technology, MC 139-74, 1200 East California Boulevard, Pasadena, CA 91125; and §Department of Radiology, Laboratory for Preclinical Imaging and Imaging Technology, University of Tübingen, Roentgenweg 11, 72076 Tübingen, Germany

Communicated by Michael E. Phelps, University of California School of Medicine, Los Angeles, CA, December 11, 2007 (received for review May 15, 2007)

Positron emission tomography (PET) and magnetic resonance imaging (MRI) are widely used *in vivo* imaging technologies with both clinical and biomedical research applications. The strengths of MRI include high-resolution, high-contrast morphologic imaging of soft tissues; the ability to image physiologic parameters such as diffusion and changes in oxygenation level resulting from neuronal stimulation; and the measurement of metabolites using chemical shift imaging. PET images the distribution of biologically targeted radiotracers with high sensitivity, but images generally lack anatomic context and are of lower spatial resolution. Integration of these technologies permits the acquisition of temporally correlated data showing the distribution of PET radiotracers and MRI contrast agents or MR-detectable metabolites, with registration to the underlying anatomy. An MRI-compatible PET scanner has been built for biomedical research applications that allows data from both modalities to be acquired simultaneously. Experiments demonstrate no effect of the MRI system on the spatial resolution of the PET system and <10% reduction in the fraction of radioactive decay events detected by the PET scanner inside the MRI. The signal-to-noise ratio and uniformity of the MR images, with the exception of one particular pulse sequence, were little affected by the presence of the PET scanner. *In vivo* simultaneous PET and MRI studies were performed in mice. Proof-of-principle *in vivo* MR spectroscopy and functional MRI experiments were also demonstrated with the combined scanner.

molecular imaging | small animal imaging | multimodality imaging

Positron emission tomography (PET) noninvasively images the distribution *in vivo* of biomolecules (small molecules, peptides, antibodies, and nanoparticles) labeled with radionuclides that undergo positron decay and produce back-to-back 511-keV annihilation photons (1). Because of the high sensitivity of radioactive assays, PET can measure picomolar concentrations of labeled biomolecules. A wide variety of molecular targets and pathways have been imaged by using PET radiotracers (2, 3), with the avid accumulation of the radiotracer [^{18}F]-2-fluoro-2-deoxy-D-gluocse (FDG) in malignant tumors being just one example that has widespread applications in the clinic and in the study of therapeutic strategies for tumor treatment in animal models. However, the spatial resolution of PET is limited by physical factors associated with positron physics and by the difficulty of acquiring sufficient counting statistics. Furthermore, PET images often lack definitive anatomic information, making interpretation of the precise location of radiotracer accumulation difficult.

Magnetic resonance imaging (MRI) can provide high-spatial-resolution anatomic images with exquisite soft-tissue contrast by exploiting the differences in relaxation times of protons in different biochemical environments (4, 5). The combination of high spatial resolution and contrast allows the anatomic consequences (e.g., tumor growth, brain atrophy, cardiac wall motion abnormalities) of many disease processes to be visualized in patients and in animal models. Functional MRI techniques can measure important physiologic parameters, including diffusion (6, 7), permeability (8), and changes in blood oxygenation levels after neuronal activation (9–11). The addition of passive contrast agents based on gadolinium or iron-oxide nanoparticles can further enhance contrast (12). A number of laboratories are also developing targeted MRI contrast agents (13–15). MR spectroscopy (MRS), which measures the shift in the frequency at which protons in different chemical environments resonate, allows the relative concentrations of abundant metabolites, and some drugs administered at mass levels, to be measured. With localized MRS, coarse spectroscopic images also can be obtained (16, 17). Proton MRS is particularly useful in tumor studies and also offers information about neuronal integrity in neurodegenerative disorders (18–21). However, the molar sensitivity of MRI for different metabolites and tracers is many orders of magnitude lower than that of PET, imposing significant restrictions on the kinds of targets that can be visualized.

Clear synergies exist between the two modalities, because each can provide unique information not attainable with the other modality. For this reason, MRI and PET are frequently combined in clinical diagnostics and research. Relevant to this work, these modalities have been increasingly used in more basic biomedical research, particularly in efforts to understand the etiology and evolution of human diseases in appropriate animal models (commonly mice and rats) and in the preclinical evaluation of new therapeutic strategies, including small-molecule drugs, peptides and antibodies, cellular therapies, gene therapy, and nanoparticle-based therapies. In particular, these modalities can be used in combination to study both the pharmacokinetics and pharmacodynamics of new therapeutics.

To date, PET and MR images are acquired on separate imaging systems and typically coregistered by using software that makes use of the information content of the image data (e.g., landmarks) or external fiducial markers that can be clearly identified in the two images (22). This approach works well in the brain, where the skull constrains movement and enables simple rigid body registration methods to be used (23). However, it becomes more problematic in the thorax, abdomen, and pelvic regions, where tissues and organs deform based on the position of the subject in the scanner, and where temporal changes such as emptying of stomach contents, movement of the food through

Author contributions: C.C., D.P., Y.W., M.S.J., B.J.P., R.E.J., and S.R.C. designed research; C.C., D.P., and Y.W. performed research; J.Q. contributed new reagents/analytic tools; C.C., D.P., Y.W., M.S.J., J.Q., B.J.P., R.E.J., and S.R.C. analyzed data; and C.C. wrote the paper.

The authors declare no conflict of interest.

Freely available online through the PNAS open access option.

†To whom correspondence should be addressed at: Athinoula A. Martinos Center for Biomedical Imaging, Department of Radiology, Massachusetts General Hospital, Building 149, Room 2301, 13th Street, Charlestown, MA 02129. E-mail: ccatana@nmr.mgh.harvard.edu.

This article contains supporting information online at www.pnas.org/cgi/content/full/0711622105/DC1.

the intestinal tract, and filling of the urinary bladder also confound registration. Deformable image registration techniques can be used, but their success is highly situation-dependent, and they are not generally robust in the presence of significant tissue movement between the two separate imaging studies. Simultaneous acquisition, therefore, would guarantee spatial registration of the two datasets.

More crucially, sequential PET and MRI scanning does not permit temporal correlation of PET and MRI studies. Biological systems are inherently dynamic, and their response to drugs and contrast agents is strongly time-dependent. The biodistribution of most contrast agents and drugs exhibits changes on time scales of seconds to minutes. To ensure that a subject is being imaged in the same physiologic state, and to correlate changes over time in the PET and MRI signals in response to an intervention, thus often requires that the data be acquired simultaneously. To give just one example, one might want to monitor dynamic changes in tumor physiology with MRI [e.g., cellularity by diffusion measurements (24), macromolecular environment (25, 26), vasculature by contrast enhancement (27)] while imaging the delivery of a radiolabeled therapeutic agent to, or assessing the biochemistry of, the tumor. Simultaneous acquisition of PET and MRI data by using an integrated imaging device is, therefore, necessary to answer many important biomedical questions in dynamic, living systems.

In designing an integrated scanner for simultaneous PET and MR imaging, an obvious challenge relates to the ways in which the PET and MRI systems can interfere with each other, leading to major artifacts and/or image degradation. The primary concerns are electromagnetic interference (EMI) and the effect of the main magnetic field (B_0) of the MRI on the detectors in the PET scanner; however, other, more subtle, effects that need to be considered include the induction of eddy currents, susceptibility artifacts, and an increase in temperature or vibrations induced by the running of MR sequences. The detectors [usually based on scintillators coupled to photomultiplier tubes (PMTs)] and associated electronics commonly used in PET scanners are sensitive to magnetic fields and contain conducting and radio-frequency (RF) radiating components that have the potential to interfere with the MRI system. For instance, PMTs are affected by even weak magnetic fields. The PET electronics can also easily pick up the strong RF signals generated by the RF coil in the MRI. Furthermore, the B_0 homogeneity in MRI must not be significantly degraded by the introduction of diamagnetic or paramagnetic materials and, where possible, any materials introduced into the magnet should be arranged symmetrically to minimize possible artifacts. Because of their high susceptibility, ferromagnetic materials are not normally useful, or even tolerable, within the magnetic field of the MRI and consequently are to be avoided.

The very earliest approaches to developing MRI-compatible PET systems used very long optical fiber connections between the scintillator elements and the PMT to effectively eliminate EMI between the two systems (28, 29). Although this led to proof-of-principle data, including a small number of animal studies, the performance of the PET scanner was poor compared with stand-alone PET scanners, and the length of the optical fibers made the system cumbersome. A variation on this design (30), using a split magnet in which the PET detectors reside in the gap and the fibers emanate radially from the magnet, offers the prospect of improved PET performance, albeit still limited by the transmission of scintillation light through very long optical fibers and the low field strength of the magnet compared with most preclinical MRI scanners.

We opt for a different approach in developing a PET scanner insert that is compatible with existing high-field animal MRI systems. We use magnetic field-insensitive avalanche photodiode (APD) detectors in place of PMTs and use very short optical fiber bundles to appropriately position the photodetectors and PET electronics with respect to the MRI RF and gradient coils, to minimize interference. A detailed description of the construction of the MRI-compatible PET insert was published in ref. 31. In brief, the PET insert comprises 16 detector modules arranged in a symmetric ring. Each PET detector module consists of an array of lutetium oxyorthosilicate (LSO) detectors coupled through a bundle of bent optical fibers to a position-sensitive APD (PSAPD) and charge-sensitive preamplifiers mounted on a printed circuit board populated with nonmagnetic components. All 16 modules are mounted on a carbon fiber tube, and the crystals in the LSO arrays form eight complete detector rings at the center of the insert [see supporting information (SI) Fig. 5*A*]. The PSAPDs and photodetectors are shielded by a copper laminate and are located in the MRI scanner such that they are axially outside of the linear region of the *z*-gradient field and outside of the imaging volume defined by the RF coil (SI Fig. 5*B*). The detectors are cooled to −10°C using chilled dry air to obtain optimal signal-to-noise from the PSAPDs and to minimize temperature drift. Details of the PET insert geometry are provided in SI Table 1. The PET insert is compatible with existing preclinical MRI scanners having a clear bore of 12 cm or greater (SI Fig. 5*C*). The PET insert is positioned in the MRI scanner by using a registration scan with PET- and MRI-visible fiducial markers such that the isocenters of the PET and MRI fields of view (FOVs) are coincident. The PET insert is readily removed, allowing it and the MRI scanner to be used as independent devices.

Other groups have pursued similar approaches but without the optical-fiber connection, placing the APDs and electronics in the active MR imaging volume (32, 33). This approach will improve PET performance by eliminating scintillation light loss in the optical fibers; however, the proximity of the APDs to the RF coil and gradients have the potential to increase interference between the systems, especially for MRI pulse sequences that demand intensive gradient-switching and high-intensity RF pulses.

Here we describe detailed phantom experiments performed with our MRI-compatible PET instrument to demonstrate that PET and MR images can be acquired simultaneously without significant interference between the two modalities. We also carried out a number of proof-of-principle *in vivo* studies to highlight the biomedical applications for this technology.

Results and Discussion

MRI System Effects on PET Imaging. Experiments to examine the interference between the two imaging systems when acquiring PET and MR data simultaneously were designed to characterize the effect of one system's image acquisition protocol on the other. PET detector maps (which show a histogram of the events detected by the 8 × 8 scintillator elements in a particular PET detector module when it is uniformly irradiated with a source of 511-keV annihilation photons) demonstrate a small rotation (clockwise or anticlockwise, depending on the orientation of the PSAPD with respect to the magnetic field) when the PET insert is inside the magnet (Fig. 1 *A* and *B*), due to the magnetic force on electrons moving through the silicon. However, the ability to resolve the detector crystals, which is a key factor contributing to the spatial resolution in PET, was not appreciably altered in the 7-T magnet.

Acquiring an MR image requires the use of strong RF pulses and rapidly switched magnetic field gradients that have the potential to perturb the weak electronic signals produced by the PET detectors. Therefore, PET measurements were taken while running MRI sequences that are normally used in small-animal studies, such as RARE (rapid acquisition with relaxation enhancement) and FLASH (fast low-angle shot). RARE is a fast spin echo (SE) sequence in which a number of 180° rephasing

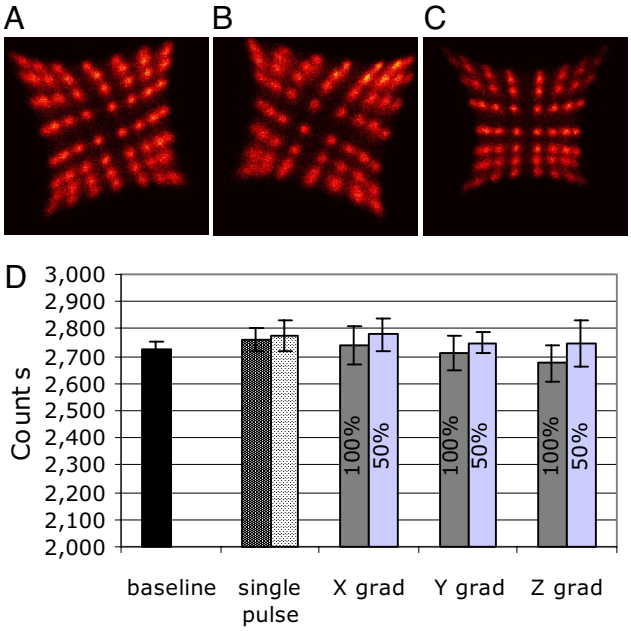

Fig. 1. MR scanner effect on PET system. (*A–C*) Detector histograms showing the anticlockwise (*A*) and clockwise (*B*) rotations of the crystal maps when compared with the data acquired outside of the magnet (*C*). (*D*) PET event rate measured under different conditions: (*i*) while applying only RF power (with 1,000 ms and 500 ms repetition times) and (*ii*) while switching the *x–z* gradients independently (at 100% and 50% power; 400 and 200 mT/m, respectively). Baseline represents the event rate recorded without running MR sequences.

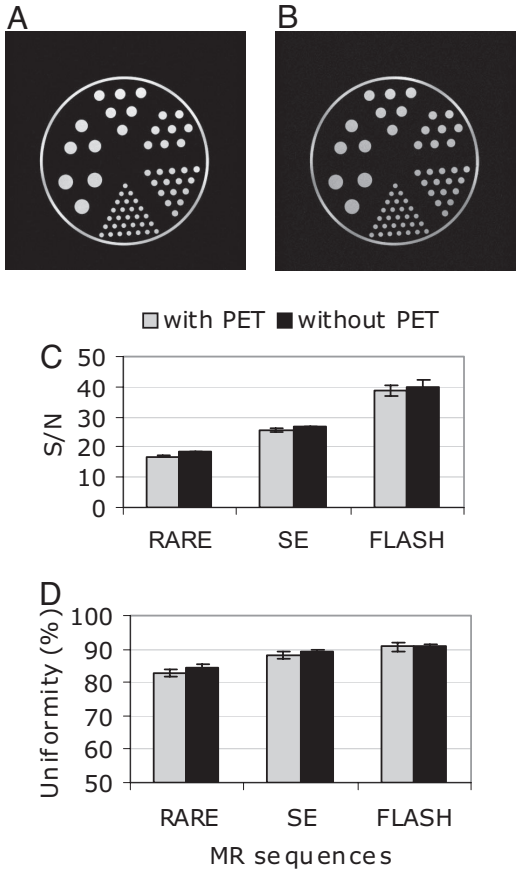

Fig. 2. PET insert effects on MR imaging. (*A* and *B*) SE (*A*) and GE (*B*) images of a structured phantom acquired in the presence of the PET insert. (*C* and *D*) SNR (*C*) and uniformity (*D*) measured for several pulse sequences with and without the PET insert, using a uniform phantom.

pulses are applied after each 90° excitation pulse to create an echo train. FLASH is based on a gradient echo (GE) sequence in which a low flip angle and a very fast repetition rate are used.

No difference in spatial resolution [expressed in terms of full-width-in-half-maximum (FWHM)] of the PET scanner could be observed when operated in the MRI scanner with RARE (1.18 ± 0.02 mm), SE (1.19 ± 0.01 mm), or FLASH (1.19 ± 0.01 mm) pulse sequences versus the spatial resolutions of 1.19 ± 0.01 mm measured within the magnet without running pulse sequences. This demonstrates that there is no observable spatial distortion of the PET data in the MRI environment. The energy resolution of the PET detectors (which is important for rejecting annihilation photons that have inelastically scattered in the body and lost their positional information) is also unchanged during MRI pulse sequences (SI Table 2). The measured absolute sensitivity (fraction of radioactive decays leading to a detected event in the PET scanner) of the PET insert was 0.6% at the center of the FOV (CFOV). No change in sensitivity was detected while running a standard SE sequence. However, a 10% and 7% decrease in event rate was observed while running the FLASH and RARE sequences, respectively. This suggests that a small fraction of events are removed from the PET data stream. Further experiments in which RF excitation and gradient switching were applied separately revealed that the effect is likely caused by the gradient switching (Fig. 1*D*). This interference only occurs over a small fraction of the duty cycle of the pulse sequence, and these events are rejected by the PET scanner because they do not meet the pulse-height criteria.

PET System Effects on MR Imaging. The presence of the PET insert in the magnet has the potential to cause artifacts or to degrade the signal-to-noise ratio (SNR) in the MR signal, both of which would reduce image quality. Therefore, MR images were compared with and without the PET insert. MR images of a structured phantom acquired in the presence of the powered PET insert with standard pulse sequences show no distortion and no obvious artifacts (Fig. 2 *A* and *B*). Subtracted images, in the presence of the powered and unpowered PET insert, demonstrate a featureless noise background (SI Fig. 6). In a separate experiment, average SNR (Fig. 2*C*) and image uniformity (Fig. 2*D*) were measured with and without the PET insert for different pulse sequences, using a homogeneous phantom. The largest decrease in SNR caused by the PET insert was with the RARE sequence (−8%, $P = 0.0001$), whereas a smaller decrease (−3%, $P = 0.0001$) was observed for the SE sequence. Similarly, the largest decrease in uniformity was noted for the RARE sequence (−2%). Smaller changes (−1%) were observed for the SE sequence and no changes were noted for the FLASH sequence.

***In Vivo* Small-Animal Simultaneous PET and MR Imaging.** *In vivo* mouse imaging studies revealed that the combined multimodality system produces consistent information in a real-world setting. A mouse injected with 10^6 MC38 cells was imaged after 10 days, when the tumor had reached ≈9 mm in diameter. Simultaneous imaging with FDG PET and anatomic MRI (Fig. 3*A*) shows a hyperintense focus of FDG uptake coincident with the tumor site. Uptake is heterogeneous, and a region of hyperintensity on MRI close to the center of the tumor shows low FDG uptake (see arrow in Fig. 3*A*), likely indicative of necrosis. This example shows the potential for combined PET/MRI studies to improve the interpretation of cancer imaging studies in heterogeneous tumors containing malignant tissue,

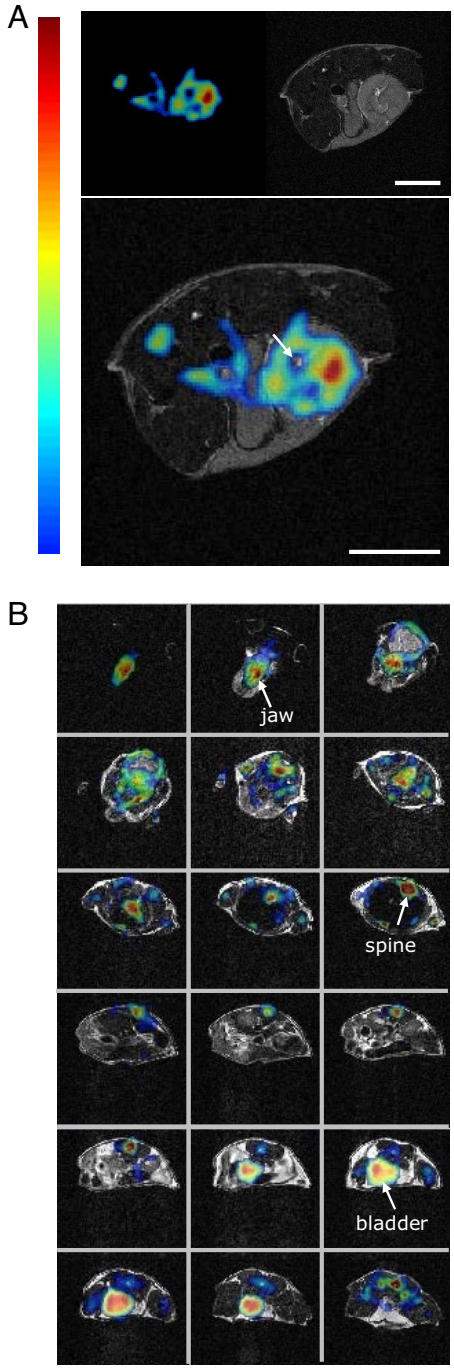

Fig. 3. Simultaneous *in vivo* PET and MR imaging. (*A*) Mouse FDG tumor imaging. (*Upper Left*) PET image, (*Upper Right*) MR image, and (*Lower*) fused PET and MR image. One transaxial image slice is shown. (*B*) Fused PET and MR images of a mouse. Transaxial sections from top of head to bladder are shown. (Scale bars, 5 mm.) The same false-color look-up table is used in both *A* and *B*.

necrosis, and edema that are not separable by MRI. Whole-body animal imaging is important in many studies (e.g., cell tracking, imaging of primary metastasis, immunological responses in cancer, and vascular plaque detection). Although the axial FOV of the MRI-compatible PET insert is just 12 mm, whole-body imaging was achieved by moving the animal bed through the two imaging systems and acquiring data that spanned the entire animal (Fig. 3*B*). This is analogous to the way in which human whole-body imaging is done by PET. The radiotracer administered was $Na^{18}F$. The ^{18}F-fluoride ion accumulates in the bony structures because of its metabolic incorporation into appetite crystals. The jaw is clearly visible in the top row, the spine can be traced through the last 10 slices, and the bladder is seen to accumulate cleared ^{18}F. MR and PET images show excellent registration along the whole body axis. This example shows the potential of the system for whole-body studies of the biodistribution of radiotracers, and the particular use of ionic ^{18}F is relevant to the use of PET/MRI to study the skeletal system in models of osteoporosis, arthritis, and bone metastasis.

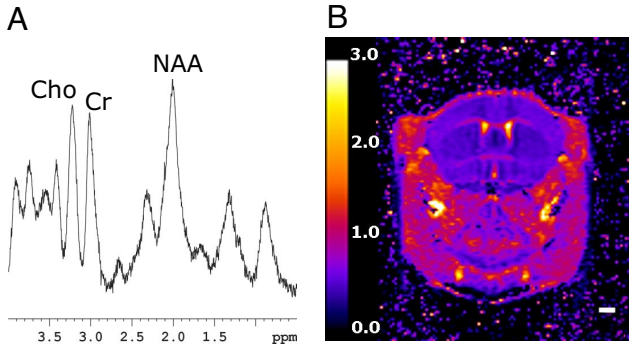

Fig. 4. Advanced MR measurements. (*A*) *In vivo* MR spectroscopy; mouse ^1H brain spectrum acquired in the presence of the PET insert. (*B*) ADC map of an *in vivo* mouse brain acquired by using a four-shot EPI sequence in the presence of the PET insert. ADC units are 10^{-3} mm^2/sec. (Scale bar, 2 mm.)

Beyond Morphological MRI: Advanced MR Techniques Performed in the Presence of the PET Insert. MRS moves MR methods into the realm of metabolic measurements, allowing the signal of abundant metabolites to be imaged, albeit on a fairly coarse spatial scale. The combination of PET and MRS measurements, therefore, also offers many opportunities. To demonstrate that MRS can be performed in the presence of the powered PET insert, a proton spectrum was acquired from a cubic voxel of size $3 \times 3 \times 3$ mm^3 positioned centrally in the normal mouse brain (Fig. 4*A*). The three singlet and one doublet resonances corresponding to *N*-actetylaspartate (NAA), choline (Cho), total creatine (Cr), and lactate (LAC) peaks, respectively, can be observed in the mouse data. By acquiring these data simultaneously with PET, it would be possible to temporally correlate the dynamics of PET and MRS signals. For example, choline metabolism, which is of special interest for cancer research, could be assessed by proton MRS, and at the same time the activity of choline kinase could be studied by PET, using synthetic ^{11}C- and ^{18}F-labeled choline analogs. Additionally, the biodistribution and metabolism of fluorine-containing drugs could be studied simultaneously by a combination of ^{18}F PET in trace amounts and ^{19}F MRS in mass amounts.

One of the most demanding, yet useful, sequences for performing functional MRI (fMRI) studies is echo planar imaging (EPI). Because this sequence employs fast gradient switching and strong gradients, it is potentially one of the most difficult to perform in the combined system. As a proof of principle, two-dimensional, four-shot EPI with diffusion-weighted images (DWI-EPI) was achieved in the presence of the PET insert. DWI is based on measuring the motion of the water molecules in biological tissues, and diffusion maps can be obtained by measuring the apparent diffusion coefficients (ADCs) for all of the voxels in the region of interest. Fig. 4*B* shows the ADC map calculated from five DWIs of a live mouse brain (see SI Fig. 7 for the individual images). The fidelity of the ADC map to literature values (34) illustrates that the PET insert has no major effect on the performance of the MR instrumentation, even

under these demanding conditions. DWI methods have proved important for assessing the pathological processes in a number of conditions, such as stroke and cancer. The combination of PET and fMRI measurements would allow different phases of a complex pharmacological response to be interrogated. For example, PET radiolabeled substrates and ligands could be used to study the rate of dopamine synthesis, transport, and receptor expression, while fMRI is used to study neuronal activation after amphetamine or cocaine stimulation.

In conclusion, we have demonstrated the feasibility of simultaneous PET and MRI studies, showing that, with proper design, no major artifacts or loss in performance are seen across a range of typical MR imaging conditions. Thus, either of the two imaging systems performs essentially the same, whether the other is present or not. We cannot exclude at this stage the presence of subtle artifacts from second-order effects that may result in small changes in signal-to-noise in one or both modalities. Nevertheless, high-quality simultaneous PET and MR studies have been demonstrated both in phantoms and *in vivo*. A number of challenges remain. Although the PET scanner performance is not unduly affected by the MRI system, the design of this prototype, in terms of sensitivity, only approximates that of first-generation animal PET scanners developed in the late 1990s (although this is still sufficient for many interesting studies). To design a MR-compatible insert that is competitive with current stand-alone PET systems will require a longer axial FOV and more efficient detectors. The use of thicker, depth-encoding detectors and a scanner design that doubles the axial FOV, leading to a >8-fold increase in sensitivity, should be explored. With the exception of this issue, there is no reason that the technology developed here cannot be translated for imaging of larger subjects, including humans.

In this work, we demonstrate that simultaneous PET and MRI scanning is both feasible and practical in the realm of small-animal imaging. *In vivo* rodent imaging presented here supports the potential for this multimodal imaging methodology in a number of applications, including the tracking of molecules and cells, pharmacokinetic/pharmacodynamic studies of drug–tissue interactions, and the functional response (via fMRI) to neuroreceptor occupancy (via PET). Merging these two modalities allows us to exploit, in a synergistic fashion, the tremendous strengths of both techniques.

Materials and Methods

PET Measurements. ***Detector maps and energy resolution.*** A ^{68}Ge source placed at the CFOV uniformly irradiated the PET detector modules. Events were sorted into 2D position histograms—detector crystal maps—that relate coordinates in the histogram to the crystal of interaction. The detector contains 64 scintillator crystals arranged in an 8 × 8 array. Events for each crystal were extracted, and a histogram of the pulse amplitudes for each crystal was plotted to determine the energy resolution (FWHM of the 511-keV photopeak divided by the photopeak amplitude). The detector maps and energy resolution for several individual crystals were measured with and without the effects of the MRI system.

PET reconstructed spatial resolution. Small-diameter (o.d./i.d. = 1.2/0.6 mm) capillary tubes filled with 25 μCi of ^{18}F were used to assess the effect of the MRI on the spatial resolution of the PET insert. PET data were acquired with and without MRI pulse sequences. The datasets were sorted into sinograms and reconstructed with a 2D filtered back-projection algorithm using a Shepp–Logan filter cut off at the Nyquist frequency. Normalization was performed using detector efficiencies estimated from a scan of a uniform cylindrical phantom. The spatial resolution was measured at the CFOV and at a 10-mm radial offset. Radial and tangential profiles were drawn through the maximum intensity pixel in the reconstructed images, and the FWHM of the point spread function was determined.

PET sensitivity measurements. A 20-μCi ^{18}F point source in a glass capillary tube was used to determine the relative sensitivity of the scanner. At the CFOV, the effect of pulse sequences was studied by recording the number of detected events while running RARE, SE, and FLASH, applying only RF power, and while switching the *x–z* gradients independently (at 100% and 50% power). The event rates under different conditions were compared by using a two-tailed Student *t* test.

MR Measurements. ***MR system.*** A Bruker 7-Tesla Biospec small-animal MR scanner, equipped with the Bruker B-GA12 gradient coil set (12 cm i.d., 40 G/cm maximum, 0.2 G·cm·Å), was used for all of the experiments described. In addition to the standard Bruker 35-mm RF coil, a custom-made whole-body mouse imaging coil with heating stage for the animal was developed for this project. The homogeneous imaging region for this coil is ≈9 cm.

MR phantom imaging. The Ultra-Micro Hot Spot Phantom (Data Spectrum) was filled with a solution of Prohance (Bracco Diagnostics) in water (T1 = 750 ms, T2 = 180 ms) and used to acquire high-resolution MR images in the presence of the powered PET insert. The diameter of the hollow channels was 0.75, 1.0, 1.35, 1.7, 2.0, and 2.4 mm, and the center-to-center spacing of the channels was 2× the diameter. Standard SE and GE sequences were run. The matrix size was 512 × 512 with a FOV of 4 × 4 cm^2.

Signal-to-noise and uniformity measurements. A uniform signal-producing cylinder (2.8 cm long, 2.8 cm i.d.) filled with Prohance in was water positioned at the isocenter of the gradient set. The signal and noise were measured in a region of interest (ROI) placed centrally on the MR image. The ROI was chosen to be small enough to avoid any significant contribution from nonuniformity. Two scans were acquired sequentially with the same parameters, and the images were subtracted. The signal was estimated as the mean pixel value in one of the images and the noise as the standard deviation of the pixel values in the difference image.

For uniformity measurements, a large ROI placed centrally on the image and avoiding the edges was chosen, and the uniformity (U) was calculated with the formula $U = 100 \times [1 - (ROI_{max} - ROI_{min})/(ROI_{max} + ROI_{min})]$, where ROI_{max} is the maximum signal intensity in the region and ROI_{min} is the minimum signal intensity in the region. The measurements were repeated for axial, coronal, and sagittal slices, while running standard SE, RARE, and FLASH sequences, with and without the PET insert present. In each case, 25 contiguous slices were defined (slice thickness 0.750 mm), and the matrix size was 256 × 256 with a 35 × 35 mm^2 FOV. Data were analyzed by using ImageJ software (National Institutes of Health). The results were compared by using a two-tailed Student *t* test.

In Vivo **Animal Studies.** ***PET/MR data acquisition setup.*** For each of the 16 PET detector modules, the lower level discriminator was set just above the noise level. The coincidence timing window was set to 50 ns, and, except for basic normalization of detector efficiencies by using a uniform cylindrical phantom, no other corrections were applied to the PET data. The PET images were reconstructed by using a fully 3D ML–EM algorithm (35) and fused with the MR images that were acquired simultaneously. The voxel size in all cases was 0.35 × 0.35 × 0.75 mm^3.

For the MR data acquisition, the coil was tuned and matched to its optimum before each experiment. First-order shimming was performed using an automatic procedure. In all cases, the sequence parameters (i.e., repetition time and number of excitations) were adjusted such that the acquisition times of the PET and MR data were similar.

Animal preparation. All animal experiments were performed under a protocol approved by the California Institute of Technology and University of California, Davis, Animal Care and Use Committees. The temperature inside the coil where the animal was placed was maintained at 37°C, and respiration was monitored. The mice were anesthetized by isoflurane inhalation (1% in 100% oxygen, IsoFlo; Abbot Laboratories).

Tumor imaging. A mouse with a flank tumor (10^6 MC38 cells injected 10 days before imaging) was injected with 200 μCi of FDG and scanned in three bed positions. A total of ≈2 × 10^6 events were included in the reconstruction. The MR data were acquired simultaneously by using the whole-body imaging coil. No respiratory gating was performed. A RARE sequence with TR/TE = 1,000/12.5 ms was used to acquire 25 slices (slice thickness 0.75 mm) with a FOV = 4 × 4 cm^2 and matrix size = 256 × 256.

Whole-body imaging. To demonstrate the feasibility of this combined system for performing whole-body imaging, a mouse was injected with ≈200 μCi of $Na^{18}F$. The mouse was positioned inside the coil, and, for each bed position, the whole setup (i.e., coil) was moved 8 mm. The bed positions were overlapped 4 mm (one-third of the FOV) to account for the decreased sensitivity toward the edge of the axial FOV, such that a total of 68 mm was covered in this direction. The data were acquired for 6 min for each bed position and corrected for radioactive decay. The MR data were acquired simultaneously, using the whole-body imaging coil. Respiratory gating was performed. A RARE sequence with TR/TE = 1,000/12.5 ms was used to acquire 31 slices (slice thickness 0.75 mm) with a FOV = 4 × 4 cm^2 and a 256 × 256 matrix size at each bed position.

In vivo *MR spectroscopy.* Volume-selective *in vivo* ^{1}H spectroscopy was performed in the presence of the powered PET insert, with a cubic voxel of $3 \times 3 \times 3$ mm^3 positioned centrally in the mouse brain. A point-resolved spectroscopy (PRESS) sequence with TR/TE = 2,500/12 ms was used. Water suppression was achieved by using a VAPOR module. The total acquisition time was 30 min.

EPI. A four-shot EPI sequence with linear ramp (ramp time = 220 μs) was used with a 25-mm head-only RF coil with TR/TE = 2,000/32 ms, bandwidth = 250 kHz, and 16 averages, for a total acquisition time of $\approx$10 min. Five slices were acquired with FOV = 1.92×1.92 cm, matrix size = 128×128, slice thickness = 0.75 mm. For diffusion weighting: $\Delta = 14$ ms; $\delta = 7$ ms; five *b* values were used (100, 200, 600, 800, and $1{,}400 \times 10^{-3}$ sec/mm^2) along the dorsoventral direction. ADC maps were calculated in the standard manner (36).

ACKNOWLEDGMENTS. We thank Kanai Shah and Richard Farrell of Radiation Monitoring Devices, Inc. (Watertown, MA) for supplying PSAPDs and for their expert advice; Drs. Yongfeng Yang and Jeff Walton for many useful discussions; Andrey Demyanenko for constructing the RF coils used in the *in vivo* imaging studies; and Dr. Andrew Raubitschek of the City of Hope Medical Center (Duarte, CA) for the MC38 tumor-bearing mouse. We gratefully acknowledge the support of the Gordon and Betty Moore Foundation to the Caltech Brain Imaging Center. This work was supported by National Institutes of Health (NIH) Grant R01 EB00993; National Center for Research Resources Grant U24 RR021760 (''Mouse BIRN''); Department of Energy Small Business Innovation Research (SBIR) Grant DE-FG02-06ER84432; NIH SBIR Grant R43 NS055377; and NIH Grant R01 EB00194 (to J.Q.).

1. Phelps ME (2004) PET: Physics, instrumentation, and scanners. *PET: Molecular Imaging and Its Biological Applications* (Springer–Verlag, New York), Chap 1.
2. Gambhir SS (2002) Molecular imaging of cancer with positron emission tomography. *Nat Rev Cancer* 2:683–693.
3. Phelps ME (2000) Positron emission tomography provides molecular imaging of biological processes. *Proc Natl Acad Sci USA* 97:9226–9233.
4. Gadian DG (1995) *NMR and Its Applications to Living Systems* (Oxford Univ Press, New York).
5. Toga AW, Mazziotta JC, eds (2002) *Brain Mapping: The Methods* (Academic, San Diego), 2nd Ed.
6. Golay X, Jiang H, van Zijl PCM, Mori S (2002) High-resolution isotropic 3D diffusion tensor imaging of the human brain. *Magn Reson Med* 47:837–843.
7. Pajevic S, Aldroubi A, Basser PJ (2002) A continuous tensor field approximation of discrete DT-MRI data for extracting microstructural and architectural features of tissue. *J Magn Reson* 154:85–100.
8. Dafni H, *et al.* (2002) MRI and fluorescence microscopy of the acute vascular response to VEGF165: Vasodilation, hyper-permeability and lymphatic uptake, followed by rapid inactivation of the growth factor. *NMR Biomed* 15:120–131.
9. Howseman AM, Bowtell RW (1999) Functional magnetic resonance imaging: Imaging techniques and contrast mechanisms. *Philos Trans R Soc London Ser B* 354:1179–1194.
10. Kim SG, Ugurbil K (2003) High-resolution functional magnetic resonance imaging of the animal brain. *Methods* 30:28–41.
11. Logothetis NK, Guggenberger H, Peled S, Pauls J (1999) Functional imaging of the monkey brain. *Nat Neurosci* 2:555–562.
12. Bulte JWM, Kraitchman DL (2004) Monitoring cell therapy using iron oxide MR contrast agents. *Curr Pharmacol Biotechnol* 5:567–584.
13. Gustafsson B, Youens S, Louie AY (2006) Development of contrast agents targeted to macrophage scavenger receptors for MRI of vascular inflammation. *Bioconjugate Chem* 17:538–547.
14. Modo M, *et al.* (2002) Tracking transplanted stem cell migration using bifunctional, contrast agent-enhanced, magnetic resonance imaging. *Neuroimage* 17:803–811.
15. Perez JM, *et al.* (2002) Magnetic relaxation switches capable of sensing molecular interactions. *Nat Biotechnol* 20:816–820.
16. Marzola P, Osculati F, Sbarbati A (2003) High field MRI in preclinical research. *Eur J Radiol* 48:165–170.
17. Nelson SJ, Vigneron DB, Star-Lack J, Kurhanewicz J (1997) High spatial resolution and speed in MRSI. *NMR Biomed* 10:411–422.
18. Morris PG (1999) Magnetic resonance imaging and magnetic resonance spectroscopy assessment of brain function in experimental animals and man. *J Psychopharmacol* 13:330–336.
19. Pathak AP, *et al.* (2004) Molecular and functional imaging of cancer: Advances in MRI and MRS. *Methods Enzymol* 386:3–60.
20. Pettegrew JW, *et al.* (2000) Molecular insights into neurodevelopmental and neurodegenerative diseases. *Brain Res Bull* 53:455–469.
21. Ross BD, Bluml S (2001) Magnetic resonance spectroscopy of the human brain. *Anat Rec* 265:54–84.
22. Hill DLG, Batchelor PG, Holden M, Hawkes DJ (2001) Medical image registration. *Phys Med Biol* 46:R1–R45.
23. Woods RP, Mazziotta JC, Cherry SR (1993) MRI-PET registration with automated algorithm. *J Comput Assist Tomogr* 17:536–546.
24. Ross BD, *et al.* (2003) Evaluation of cancer therapy using diffusion magnetic resonance imaging. *Mol Cancer Ther* 2:581–587.
25. Jones CK, *et al.* (2006) Amide proton transfer imaging of human brain tumors at 3T. *Magn Reson Med* 56:585–592.
26. van Zijl PCM, *et al.* (2003) Mechanism of magnetization transfer during on-resonance water saturation. A new approach to detect mobile proteins, peptides, and lipids. *Magn Reson Med* 49:440–449.
27. Gimi B, *et al.* (2005) Molecular imaging of cancer: Applications of magnetic resonance methods. *Proc IEEE* 93:784–799.
28. Christensen NL, Hammer BE, Heil BG, Fetterly K (1995) Positron emission tomography within a magnetic field using photomultiplier tubes and lightguides. *Phys Med Biol* 40:691–697.
29. Shao Y, *et al.* (1997) Simultaneous PET, MR imaging. *Phys Med Biol* 42:1965–1970.
30. Lucas AJ, *et al.* (2006) Development of a combined microPET-MR system. *Technol Cancer Res Treat* 5:337–341.
31. Catana C, *et al.* (2006) Simultaneous acquisition of multislice PET and MR images: Initial results with a MR-compatible PET scanner. *J Nucl Med* 47:1968–1976.
32. Grazioso R, *et al.* (2005) APD-based PET detector for simultaneous PET/MR imaging. *Mol Imaging* 4:584.
33. Judenhofer MS, *et al.* (2007) PET/MR images acquired with a compact MR-compatible PET detector in a 7-T magnet. *Radiology* 244:807–814.
34. Moffat BA, *et al.* (2006) The functional diffusion map: An imaging biomarker for the early prediction of cancer treatment outcome. *Neoplasia* 8:259–267.
35. Hu J, Qi J, Huber JS, Moses WW, Huesman RH (2005) MAP image reconstruction for arbitrary geometry PET systems with application to a prostate-specific scanner. *Proceedings of the Eighth International Meeting on Fully Three-Dimensional Image Reconstruction in Radiology and Nuclear Medicine* (Utah Center for Advanced Imaging Research, Salt Lake City), pp 416–420. Available at www.ucair.med.utah.edu/3D05/PaperPDF/3D05proceedings-part6-pages233-end.pdf (see pp 184–188).
36. Mascalchi M, *et al.* (2005) Diffusion-weighted MR of the brain: Methodology and clinical applications. *Radiol Med (Torino)* 109:155–197.